Mammalian sperm hyperactivation regulates navigation via physical boundaries and promotes pseudo-chemotaxis

Meisam Zaferani[a], Susan S. Suarez[b], and Alireza Abbaspourrad[a,1]

[a]College of Agriculture and Life Sciences, Departments of Food Science, Cornell University, Ithaca, NY 14853; and [b]College of Veterinary Medicine, Department of Biomedical sciences, Cornell University, Ithaca, NY 14853

Edited by David E. Clapham, HHMI Janelia Research Campus, Ashburn, VA, and approved September 30, 2021 (received for review April 20, 2021)

Mammalian sperm migration within the complex and dynamic environment of the female reproductive tract toward the fertilization site requires navigational mechanisms, through which sperm respond to the tract environment and maintain the appropriate swimming behavior. In the oviduct (fallopian tube), sperm undergo a process called "hyperactivation," which involves switching from a nearly symmetrical, low-amplitude, and flagellar beating pattern to an asymmetrical, high-amplitude beating pattern that is required for fertilization in vivo. Here, exploring bovine sperm motion in high–aspect ratio microfluidic reservoirs as well as theoretical and computational modeling, we demonstrate that sperm hyperactivation, in response to pharmacological agonists, modulates sperm–sidewall interactions and thus navigation via physical boundaries. Prior to hyperactivation, sperm remained swimming along the sidewalls of the reservoirs; however, once hyperactivation caused the intrinsic curvature of sperm to exceed a critical value, swimming along the sidewalls was reduced. We further studied the effect of noise in the intrinsic curvature near the critical value and found that these nonthermal fluctuations yielded an interesting "Run–Stop" motion on the sidewall. Finally, we observed that hyperactivation produced a "pseudo-chemotaxis" behavior, in that sperm stayed longer within microfluidic chambers containing higher concentrations of hyperactivation agonists.

mammalian sperm | female reproductive tract | hyperactivation | navigation | sperm–wall interactions

The navigational mechanisms that regulate sperm migration through the complex and dynamic physical and chemical environments of the female reproductive tract to the site of fertilization are poorly understood (1, 2). Over many years, studies have revealed that the biophysical navigational cues for sperm in the female tract include fluid flow (3–7), wall architecture (8–12), ambient rheological properties such as fluid viscoelasticity (13), and possible temperature gradients (14, 15). There is also evidence that biochemical cues from the female tract serve to modulate sperm migration (16). These may include chemoattractants (17, 18), molecular triggers that change sperm flagellar beating patterns (19–21), and sperm receptors on the epithelium of the tract that anchor sperm (22–24).

The in vivo biochemical factors that transform sperm flagellar beating patterns are not precisely known (16), but in vitro exposure to certain chemical stimuli results in similar transformation of the flagellar beating pattern (25). Specifically, exposure to certain chemical stimuli results in the rise of cytoplasmic Ca^{2+} in sperm (26, 27) through either activation of CATSPER membrane ion channels and flux of exogenous Ca^{2+} ions into the flagellum (28, 29) or by mobilization of intracellular Ca^{2+} stores (30–32) or both. In turn, this rise of cytoplasmic Ca^{2+} concentration results in an increase of asymmetry in the flagellar beat cycle. This process is called "hyperactivation," and it is required for fertilization (33, 34), as it enhances the ability of sperm to penetrate the matrix of the oocyte's cumulus oophorus and zona pellucida to reach the plasma membrane of the oocyte (21). Furthermore, there is evidence that hyperactivation assists sperm swimming through viscoelastic substances in the female reproductive tract (35) and plays a role in detaching sperm from epithelial cells in the oviduct (36). It has been observed that hyperactivation is stimulated via a concentration-dependent mechanism (21).

Although past findings have revealed roles that hyperactivation plays in supporting the success of fertilization, it remains elusive whether this functional state of motility is directly involved in sperm navigation within the female reproductive tract. Accordingly, we hypothesized that hyperactivation influences sperm–sidewall interactions and thus regulates sperm navigation via nearby wall architecture. Furthermore, we expected this regulatory mechanism to be dependent on the concentration of hyperactivation agonists.

Here, using microfluidic experimentation with bovine sperm as well as theoretical and computational modeling, we investigated the effect of hyperactivation on hydrodynamic sperm–sidewall interactions in both standard and viscoelastic media. We used two established pharmacological agents to trigger hyperactivation in sperm: caffeine (25) and 4-aminopyridine (4-AP) (37). We demonstrated that hyperactivation directly regulates sperm interactions with sidewalls of our microfluidic reservoirs and thus

Significance

Mammalian sperm migration within the female reproductive tract requires navigational mechanisms, through which sperm respond to biophysical and biochemical cues. Previous studies revealed that biophysical cues for sperm in the female reproductive tract include fluid flow, wall architecture, and temperature gradients. Here, by exploring bovine sperm motion in microfluidic reservoirs and by developing theoretical and computational models, we demonstrate that sperm motility hyperactivation, which is part of a process that prepares sperm in the female tract for fertilization and involves an increase in the asymmetry of sperm flagellar beating, modulates sperm–sidewall interactions and thus navigation via female tract wall architecture. Specifically, hyperactivation reduces the tendency of sperm to remain swimming along walls and promotes a response that resembles chemotaxis.

Author contributions: M.Z., S.S.S., and A.A. designed research; M.Z. performed research; M.Z. contributed new reagents/analytic tools; M.Z. analyzed data; and M.Z., S.S.S., and A.A. wrote the paper.

The authors declare no competing interest.

This article is a PNAS Direct Submission.

[1]To whom correspondence may be addressed. Email: alireza@cornell.edu.

This article contains supporting information online at http://www.pnas.org/lookup/suppl/doi:10.1073/pnas.2107500118/-/DCSupplemental.

Published October 29, 2021.

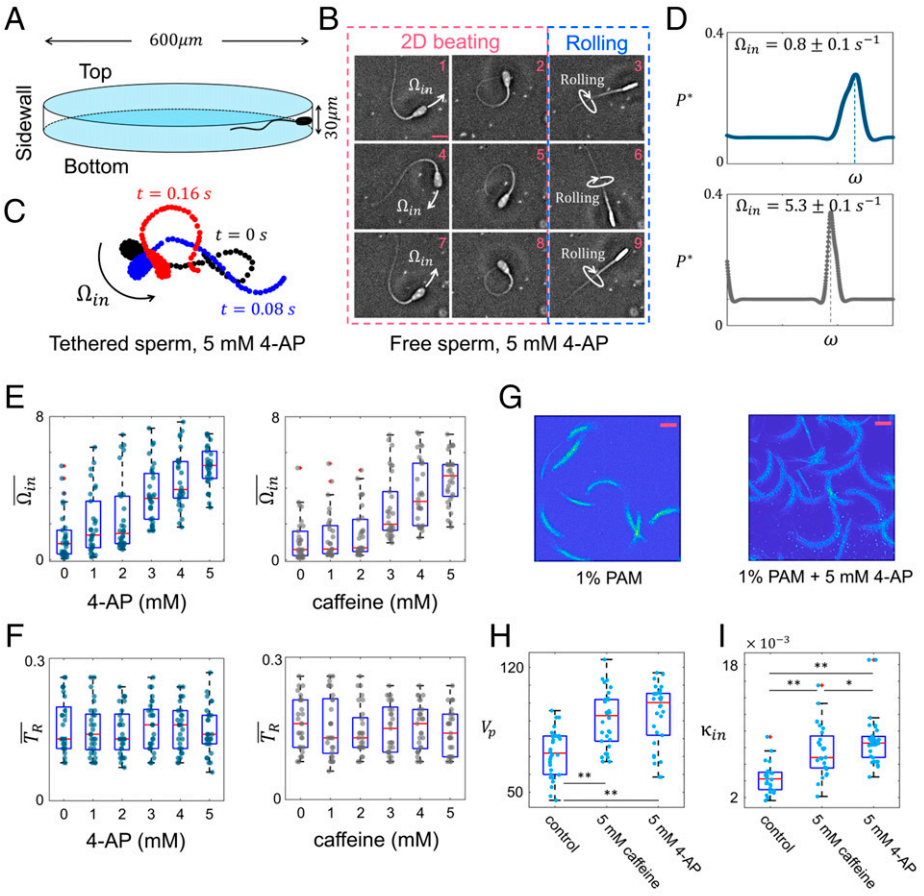

Fig. 1. Characterization of hyperactivated motility. (*A*) The microfluidic reservoir. The diameter and height of reservoir are 600 and 30 μm, respectively. (*B*) Sequential images of free sperm flagellar beating in the standard solution with 5 mM 4-AP. The time between two consecutive images is 0.08 s. (*C*) Asymmetric flagellar beating of a tethered, 4-AP–treated sperm yields rotation about the tethering point. (*D*) Existence of a zeroth harmonic in the frequency domain results in the flagellar asymmetry and thus the sperm's angular velocity about the tethering point. (*E*) $\overline{\Omega_{in}}$ increases with the concentration of treatments. (*F*) $\overline{T_R}$ remained unchanged by 4-AP or caffeine. (*G*) Circular motion of sperm in viscoelastic (1% PAM) solution with and without 5 mM 4-AP. Rolling was suppressed in the viscoelastic solution. These images were obtained by combining consecutive images taken from sperm for 200 ms at 50 frames/s. (Scale bar, 50 μm.) Treatment with 5 mM caffeine or 4-AP increased sperm propulsive velocity (*H*) and circular path curvature in the viscoelastic solution (*I*). Units of V_p and κ_{in} are $\mu m \cdot s^{-1}$ and μm^{-1}. *P value < 0.025 and **P value < 0.0001. These P values were obtained from two-tailed t tests, with adjustments for multiple comparisons (Bonferroni correction).

navigation via physical boundaries. As a result of this concentration-dependent regulatory mechanism, we observed a "pseudo-chemotaxis" phenomenon in which sperm accumulated within reservoirs with higher concentrations of hyperactivation agonists. Our results revealed a potential role of hyperactivation in the navigational response of sperm to biochemical cues within the female reproductive tract.

Results

Quantitative Characterization of Hyperactivated Motility. Our microfluidic device consisted of a main channel that was connected by smaller channels to side circular reservoirs (Fig. 1*A*). The diameter and height of the circular reservoirs were 600 and 30 μm, respectively. These dimensions were chosen to mimic the generic high–aspect ratio geometry of the sperm swimming environment in the female reproductive tract, specifically microgrooves (4) and narrow spaces between mucosal folds that line areas of the tract (*SI Appendix*, *Geometry of Sperm Environment within the Female Reproductive Tract*). We further explain the rationale for choosing a circular geometry in the next section. These circular reservoirs were filled with a standard bovine sperm medium, Tyrode albumin lactate pyruvate (TALP) medium (7), containing the agonist caffeine or 4-AP to stimulate hyperactivation. Caffeine and 4-AP were chosen as hyperactivation agonists because they have been used by various laboratories to trigger hyperactivation in bovine and other species of mammalian sperm (25, 36–38). In some experiments, 1% polyacrylamide (PAM) was also added to increase viscoelasticity of the solution (39) to model the levels present in some parts of the female reproductive tract (*SI Appendix*, *Rheological Properties of Standard and Viscoelastic Solutions*). When we injected diluted semen into the main channel, sperm showing normal motility swam along the sidewalls of the main channel and subsequently entered the reservoirs, where they became exposed to a treatment. We should note that only progressively motile sperm entered the reservoirs; immotile and weakly motile sperm remained behind near the injection point.

Motility of freely swimming sperm in a standard (nonviscoelastic) solution (TALP) with and without the treatment were seen to be composed of two components, two-dimensional (2D) flagellar beating (40) and sperm rolling about its longitudinal axis (41, 42), as shown in Fig. 1*B*. Because quantifying the flagellar beating pattern was challenging when sperm were rolling, we first suppressed the rolling component by tethering the sperm head to the bottom glass surface of the reservoir (Fig. 1*C*) to

characterize the beating pattern (43). We observed that asymmetry in the sperm flagellar beating yields a rotation about the tethering point with a time-averaged angular velocity of $\overline{\Omega_{in}}$ (Fig. 1*C* and Movies S1 and S2). While measuring the bending in the midpiece of the flagellum and taking its fast Fourier transform ($P^*(\omega)$; Fig. 1*D* and *SI Appendix*, *Sperm Flagellar Beating Pattern*), we observed that asymmetry in the flagellar beating pattern is caused by existence of a zeroth harmonic (static component) in the frequency domain of sperm flagellar beating (40).

To characterize transformation of sperm motility by caffeine or 4-AP treatments, we selected a range of 0 to 5 mM of the agonists, because our preliminary observations showed that, at caffeine or 4-AP concentrations higher than 5 mM, more than 40% of sperm became immotile (*SI Appendix*, *Motility of Agonist-Treated Sperm*). Measuring $\overline{\Omega_{in}}$ for tethered sperm at 0 to 5 mM 4-AP or caffeine, we found that these agonists increased $\overline{\Omega_{in}}$ in a concentration-dependent manner (Fig. 1*E*). According to our regression model with the least-squares approach, $\overline{\Omega_{in}} = 0.15c^2 + 1.75$ ($R^2 \approx 0.95$) for 4-AP and $\overline{\Omega_{in}} = 0.14c^2 + 1.17$ ($R^2 \approx 0.96$) for caffeine. Note that c represents the agonist concentration in mM. In contrast, $\overline{T_R}$ (the time average of the time frames between two consecutive occurrences of rolling in a sperm) did not change in the nontethered sperm in response to the treatments with 4-AP or caffeine (Fig. 1*F*). Therefore, mammalian sperm hyperactivation involves an increase of asymmetry in the flagellar beat and the corresponding $\overline{\Omega_{in}}$ without a significant change in rolling.

When we added 1% PAM to approximate viscoelasticity levels in parts of the female tract (39), sperm rolling was suppressed in most (>95%) sperm (*SI Appendix*, *Motility of Agonist-Treated Sperm*). Therefore, in the viscoelastic fluid, sperm swam in circular paths, the curvatures of which were related to the level of asymmetry in the flagellar beating pattern (40) (Fig. 1*G*). Upon hyperactivation, sperm propulsive velocity (V_p) and circular path curvature $\left(\kappa_{in} = {}^{\Omega_{in}}/_{V_p}\right)$ were increased significantly (Fig. 1 *H* and *I*), which agrees with the results shown in Fig. 1 *E* and *F*. For the sake of consistency, we refer to the sperm intrinsic curvature as κ_{in} in the rest of the manuscript. This term must not be confused with the average curvature of the sperm flagellum. Note that sperm motility featured frequent rolling in the standard solution with and without the agonist treatment. This frequent rolling appeared to counteract the effect of asymmetric beating by alternating the asymmetry direction, which resulted in progressive motion in the majority (>90%) of sperm with and without treatments (*SI Appendix*, *Motility of Agonist-Treated Sperm* and *The Effect of Rolling*).

Effect of Hyperactivation on Sperm—Sidewall Interactions. Like other microswimmers (44, 45), sperm physical interactions with nearby walls influences its motion. We observed that in both standard and viscoelastic solutions, with and without treatments, sperm swam consistently close to (<5 μm) the bottom or top surfaces, which agrees with previous studies. Because of this consistent swimming in proximity to the bottom or top surfaces, sperm motion was effectively 2D. Based on previous studies, hydrodynamic interactions between rolling sperm and these surfaces results in a circular motion (*SI Appendix*, *The Effect of Bottom (Top) Surface on Sperm Motion*). Note that this circular motion is caused by sperm frequent rollings (42) and should not be confused with the circular motion caused by asymmetry in sperm flagellar beating. To characterize this circular motion caused by rolling, we measured the average curvature of the circular motion in rolling sperm just before the sperm contacted the sidewall of the reservoirs and, as our measurements indicate, $\kappa_R = 0.8 \pm 0.3 \times 10^{-3}\ \mu m^{-1}$. Since the curvature of this circular motion is much lower than that of our microfluidic reservoirs ($\kappa_w = 3.3 \times 10^{-3}\ \mu m^{-1}$), we neglected the effect of top or bottom surfaces on sperm motion and developed simple 2D models to focus on sperm hydrodynamic interactions with sidewalls. For clarity, we refer to sperm hydrodynamic interactions with sidewalls as sidewall interactions throughout the manuscript.

In general, sperm–sidewall interactions result in stable swimming along the walls, known as boundary-following motion (8). Sidewall interactions, which are sensitive to the architectural features of the wall, are known to contribute to sperm navigation in confined spaces, such as in the female reproductive tract (4). According to our experimental measurements of sperm orientation with respect to the sidewall (*SI Appendix*, *Sperm-Wall Interaction before Contact*), we did not observe a substantial change in the orientation before sperm contacted the sidewall. Therefore, based on previous studies about hydrodynamic interactions of sperm (or bacteria) with flat sidewalls (46, 47), we developed a simple model to understand the governing physical principles of sperm–sidewall interactions, as follows. Once a high–aspect ratio swimming rod that represents a single progressively motile sperm contacts a flat sidewall, it experiences a rotation imposed by the sidewall (i.e., Ω_w), which depends on the rod angle with respect to the line perpendicular to the sidewall at the contact point (i.e., $\varphi(t)$), its propulsive velocity (i.e., V_p), and fluid properties such as viscosity (*SI Appendix*, *Sperm-Wall Interaction after Contact*). Because of the linearity of the Stokes equation, and as our simulations confirmed, Ω_w is linearly correlated with V_p, and it can be written as

$$\Omega_w = V_p \cdot g(\varphi). \qquad [1]$$

Note that $g(\varphi)$ has a dimension of curvature and describes the dynamic of the rod rotation after contacting the sidewall. Computational, theoretical, and experimental characterizations of $g(\varphi)$ validate that sperm–wall dynamics are bistable with stabilities $\varphi = \frac{\pi}{2}$, $-\frac{\pi}{2}$ and instability at $\varphi = 0$ (*SI Appendix*, *Sperm-Wall Interaction after Contact*). Consequently, sperm stably swim along the sidewall after the contact so that the direction of swimming in either $\varphi = \frac{\pi}{2}$ or $-\frac{\pi}{2}$ direction depends on the initial incidence angle.

Corners (48), where two flat sidewalls meet, and the gradient of sidewall curvature (49) influence the motion of a microswimmer on a wall. We expanded our model to study sidewall interactions in the vicinity of corners, where sperm experience the weighted superimposed effects from both sidewalls (*SI Appendix*, *Sperm-Wall Interaction after Contact*). Our expanded model suggested that when a sperm that is swimming along a flat sidewall encounters an acute angle corner, the sperm cannot pass across the corner and thus fails to begin swimming along the adjacent sidewall. However, as a corner's angle increases and becomes wide, sperm eventually pass across the corner, reorient to become parallel to the adjacent sidewall, and begin swimming along it. The time required for sperm to reorient at corners results in slower motion and temporary accumulation of sperm within the corner. However, sperm velocity and thus distribution are uniform around a circular sidewall with zero gradient of sidewall curvature and no corners. To experimentally verify the results obtained from our model, we combined frames of the videos acquired from sperm in the standard solution within triangular, square, pentagonal, hexagonal, and circular reservoirs and measured the optical intensity of the sperm layer formed on the perimeter of each reservoir. The optical intensity of the sperm layer verified the accumulations of sperm at the corners and uniform distribution around the circular sidewall (*SI Appendix*, Fig. S12).

To study the effect of hyperactivation on sidewall interactions, a circular reservoir was chosen as it eliminated the temporary accumulations and complexities associated with corners and curvature gradients in the sidewalls. Accordingly, our observations are solely caused by the influence of hyperactivation on sperm–sidewall

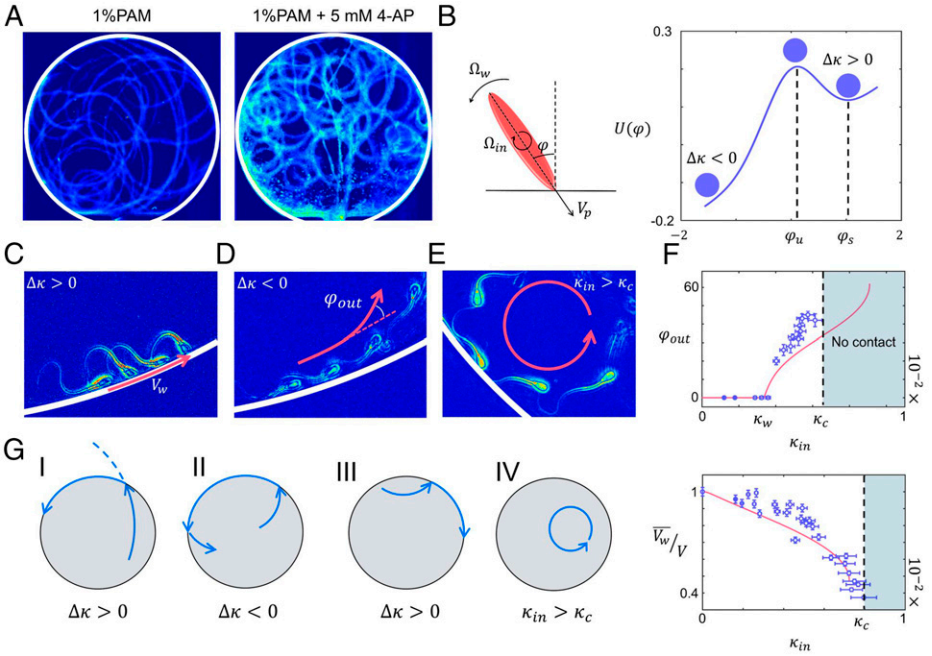

Fig. 2. Effect of hyperactivation on sperm–sidewall interactions. (*A*) Time projection of sperm motion in viscoelastic solutions with and without 5 mM 4-AP. These images were obtained by combining frames acquired from sperm (25 frames/s) within circular reservoirs over 1-min periods. (*B*) Modeling sperm as a high–aspect ratio rod, the defining potential function of sperm–sidewall interactions is bistable, and sperm swimming behavior on the sidewall depends on the magnitude and sign of its intrinsic curvature (Ω_{in}/V_p) at the contact point. *x*-axis, φ, Ω_{in}, V_p, and Ω_w are depicted in the schematic. For $\Delta\kappa > 0$, a sperm swims along the sidewall (*C*), while for $\Delta\kappa < 0$, a sperm detaches after a temporary retention on the sidewall (*D*). (*E*) For $\kappa_{in} > \kappa_c$, no swimming along the sidewall occurs. Images shown in *C*, *D*, and *E* are obtained by combining four images taken from sperm at 100-ms intervals. (*F*) For $\Delta\kappa < 0$, sperm velocity on the wall, and for $\Delta\kappa > 0$, detachment angle with respect to the intrinsic curvature. The solid red line is obtained from simulation, while blue dots represent experimental measurements. Error bars are used to indicate the estimated error in a measurement. The units for φ_{out} and κ_{in} are degrees and μm^{-1}. (*G*) Four categories of sperm–sidewall interactions.

interactions rather than geometrical features on the sidewall. Furthermore, because the diameter of the circle (600 μm) was much greater than sperm length (50 μm), we could approximate the sidewall as a plane in our models of sperm–sidewall interactions.

In viscoelastic solutions, in which the rolling component was suppressed, the curvature of the sperm's circular path increased with hyperactivation as expected (Fig. 2*A*). Consequently, fewer wall contacts and interactions occurred with hyperactivation, even after long periods of observation (~10 min). For the sake of simplicity, we first characterized sperm hydrodynamic interactions with the sidewall when rolling was suppressed (*SI Appendix, Reciprocal Theorem and the Effect of Intrinsic Curvature*). Recalling that $g(\varphi)$ describes the dynamic of interactions between progressive sperm and sidewall after contact, $g^*(\varphi)$ (Eq. **2**) captures the influence of sperm intrinsic curvature (κ_{in}) in the dynamic.

$$g^*(\varphi) = g(\varphi) + \kappa_{in}\left(1 + l^2 g^2(\varphi)\right), \qquad [2]$$

where l is sperm length, and κ_{in} can be positive or negative at the contact point. In Eq. **2**, we neglected the effect of sidewall curvature (κ_w) as $\kappa_w \ll (2l)^{-1}$. The defining potential function $U(\varphi) = -\int g^*(\varphi)d\varphi$ is bistable with one unstable (φ_u) and two positive and negative stable equilibrium points at φ_s (Eq. **3**) that correspond to positive and negative values of $\Delta\kappa$ (Fig. 2*B*):

$$\varphi_s = g^{-1}(\Delta\kappa), \qquad \Delta\kappa \approx \frac{-1 + \sqrt{1 - 4l^2\kappa_{in}^2}}{2l^2\kappa_{in}}. \qquad [3]$$

For $\Delta\kappa > 0$, the sperm swims along the sidewall with a final orientation of φ_s with respect to the sidewall (Fig. 2*C*), and thus, its averaged swimming velocity on the sidewall depends on $\Delta\kappa$ (i.e., $V_w = V_p \sin\varphi_s = V_p \sin\left(g^{-1}(\Delta\kappa)\right)$), whereas for $\Delta\kappa < 0$ the sperm detaches after temporarily swimming along the sidewall with an angle of $\varphi_{out} = \frac{\pi}{2} - \varphi_s$ (Fig. 2*D*). Interestingly, as the sperm intrinsic curvature increases and $|\Delta\kappa| > \max\{g(\varphi)\}$, circular motion dominates the wall effect regardless of the curvature's sign at the contact point, and consequently the sperm swims in circular paths with curvature of κ_{in} and negligibly influenced by the sidewall (Fig. 2*E*). Therefore, for sperm with intrinsic curvatures above a critical value (Eq. **4**), the sidewall interactions diminish and the sperm swim independently of nearby sidewalls:

$$\kappa_C = \max\left\{\frac{g(\varphi)}{1 + l^2 g^2(\varphi)}\right\}. \qquad [4]$$

While measuring V_w/V_p for the sperm with $\Delta\kappa > 0$ and φ_{out} for the sperm with $\Delta\kappa < 0$ (Fig. 2*F*), we found the critical value of $\kappa_C = (7.08 \pm 0.83) \times 10^{-3}\,\mu m^{-1}$. In agreement with our prior observations, 70 ± 5% of sperm with 5 mM 4-AP treatment and 60 ± 7% with 5 mM caffeine treatment exhibited $\kappa_{in} > \kappa_C$, as opposed to the control, in which 5 ± 2% exhibited $\kappa_{in} > \kappa_C$.

To summarize, the sidewall interactions for nonrolling sperm fall into four categories (Fig. 2*G*): 1) $|\kappa_{in}| < \kappa_w$, which results in $\Delta\kappa > 0$, and thus, there is stable swimming along the sidewall; 2) $|\kappa_{in}| > \kappa_w$ with $\Delta\kappa < 0$, which results in detachment after temporarily swimming along the sidewall (Movie S3); 3) $|\kappa_{in}| > \kappa_w$ with $\Delta\kappa > 0$, which results in stable but slower swimming as compared to 1) (Movie S4); and 4) wall-independent swimming, which corresponds to $\kappa_{in} > \kappa_C$ (Movie S5). Treatment with 4-AP or caffeine, resulted in more sperm falling into Category IV, in which a sperm's circular motion would not be influenced by its nearby physical side boundaries.

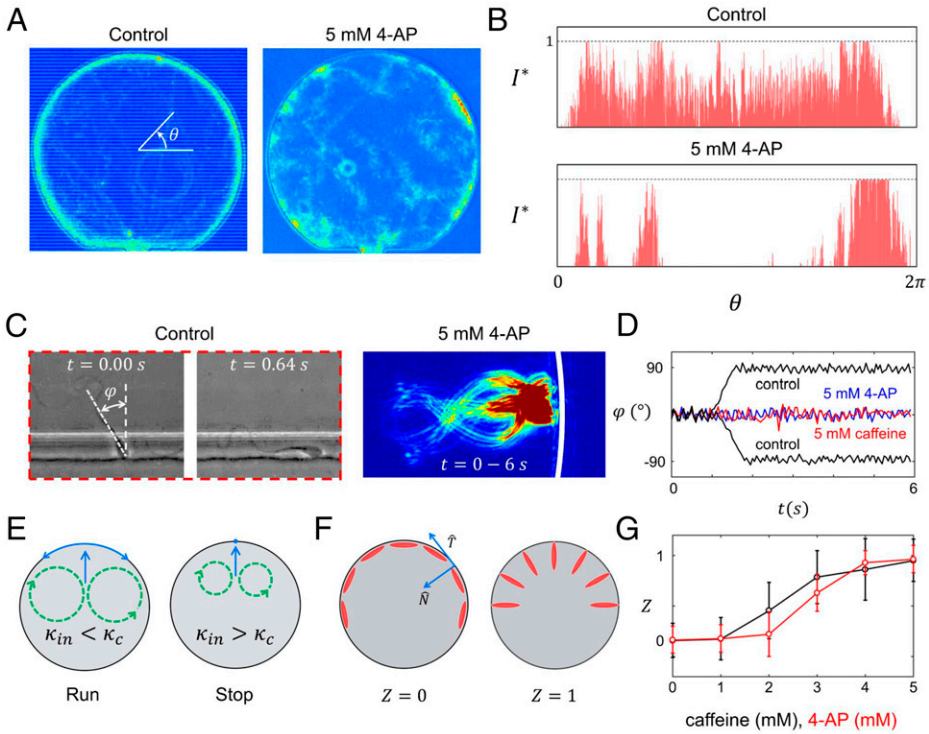

Fig. 3. Effect of hyperactivation on sperm–sidewall interactions. (*A*) Time projection of sperm motion in standard medium with and without 5 mM 4-AP. These images were obtained by combining frames acquired at (25 frames/sec) of sperm in circular reservoirs over 1-min periods. (*B*) The normalized optical density of the sperm layer formed around the circular sidewall with and without 5 mM 4-AP. The distribution of sperm around the sidewall was uniform in the control, whereas treatments with hyperactivation agonists yielded irregular accumulations along the sidewall. Similar results were obtained for 5 mM caffeine (shown in *SI Appendix*). (*C*) Rolling sperm reorientation after sidewall contact in the control medium. With 5 mM 4-AP (or caffeine), sperm maintained perpendicular orientation with respect to the sidewall. (*D*) Experimental measurements of sperm orientation with respect to the sidewall with and without treatment. (*E*) Rise of intrinsic curvature above the critical value yields Stop motion on the sidewall. Definition (*F*) and experimental measurements (*G*) of *Z* parameter at different concentrations of caffeine or 4-AP. Each point and error bar corresponds to three replicates.

Remarkably, unlike sperm in the control TALP solution, agonist-treated sperm did not distribute uniformly around the sidewalls; instead, irregular and sporadic accumulations were observed with 5 mM 4-AP or 5 mM caffeine treatments (Fig. 3 *A* and *B* and Movies S6 and S7). Furthermore, the thickness of sperm layers significantly increased with the treatment, which indicates that the angle between sperm and the sidewall had increased with onset of hyperactivation (*SI Appendix*, *Sperm-Wall Interaction with and without Treatments*).

To understand the dynamic of sidewall interactions in the standard solution, we emphasize that, in the standard solution, sperm roll frequently, which repeatedly changes the sign of κ_{in} at the contact point on the sidewall. We captured the frequent rolling in our analysis with a function $\Pi(t)$, such that $\kappa_{in}(t) = \Pi(t) \cdot \kappa_{in}$ (Eq. **5** and *SI Appendix*, *The Effect of Rolling*).

$$g^*(\varphi,t) = g(\varphi) + \Pi(t) \cdot \kappa_{in}\left(1 + l^2 g^2(\varphi)\right), \quad [5]$$

$$\overline{g^*(\varphi,t)} \approx g(\varphi). \quad [6]$$

Note that $\Pi(t=0) = 1$, and it multiplies by -1 at each incidence of rolling, which yields $\overline{\Pi(t)} \approx 0$. Accordingly, sperm–sidewall interactions alternate between Categories 2 and 3 (positive and negative $\Delta\kappa$) with each incidence of rolling, and stability shifts between φ_s and $\pi - \varphi_s$ (or $-\varphi_s$ and $\varphi_s - \pi$) frequently. Frequent shifts between φ_s and $\pi - \varphi$ (or $-\varphi_s$ and $\varphi_s - \pi$) push stability toward its mean value, which depends on κ_{in} and approaches $\frac{\pi}{2}$ (or $-\frac{\pi}{2}$) as $\kappa_{in} \to 0$. In other words, frequent rolling counteracts the influence of intrinsic curvature (13) and, thus, reduces its time-averaged effect on the sidewall interactions (Eq. **6** and *SI Appendix*, *The Effect of Rolling*). Therefore, rolling sperm reorient after contact with the sidewall and swim along it isotropically in both directions, depending on the initial sign of $\Delta\kappa$ at the moment of contact (Fig. 3 *C* and *D* and Movie S6).

However, hyperactivated rolling sperm with $\kappa_{in} > \kappa_C$ did not swim along the sidewall and maintained perpendicular orientation with respect to the wall (Fig. 3*C*, 5 mM 4-AP and Fig. 3*D*, 5 mM 4-AP and 5 mM caffeine). In a standard solution, 84 ± 5% of sperm maintained perpendicular orientation with respect to the sidewall with 5 mM 4-AP treatment and 79 ± 8% with 5-mM caffeine treatment. To understand the dynamic of sidewall interactions after hyperactivation, we recall Eq. **2**, which describes the dynamic of sidewall interactions for nonrolling sperm. Once hyperactivation results in a rise of intrinsic curvature above the critical value, the contribution of the first term of Eq. **2** in the dynamic of sidewall interactions diminishes. Thus, the dynamic of sidewall interactions for hyperactivated sperm in the presence of rolling can be written as the following:

$$g^*(\varphi,t) \approx \Pi(t) \cdot \kappa_{in}\left(1 + l^2 g^2(\varphi)\right). \quad [7]$$

Note that the time-average effect of intrinsic curvature in Eq. **7** is zero $\left(\overline{\Pi(t)} \approx 0\right)$, which yields:

$$\overline{g^*(\varphi,t)} \approx 0. \quad [8]$$

By measuring φ_{in} for 40 hyperactivated sperm, as well as solving Eq. **7**, we noticed that our model agrees with experimental observations and hyperactivated rolling sperm with $\kappa_{in} > \kappa_C$ contact the sidewall perpendicularly (because of steric repulsions) and maintain their orientation with respect to the

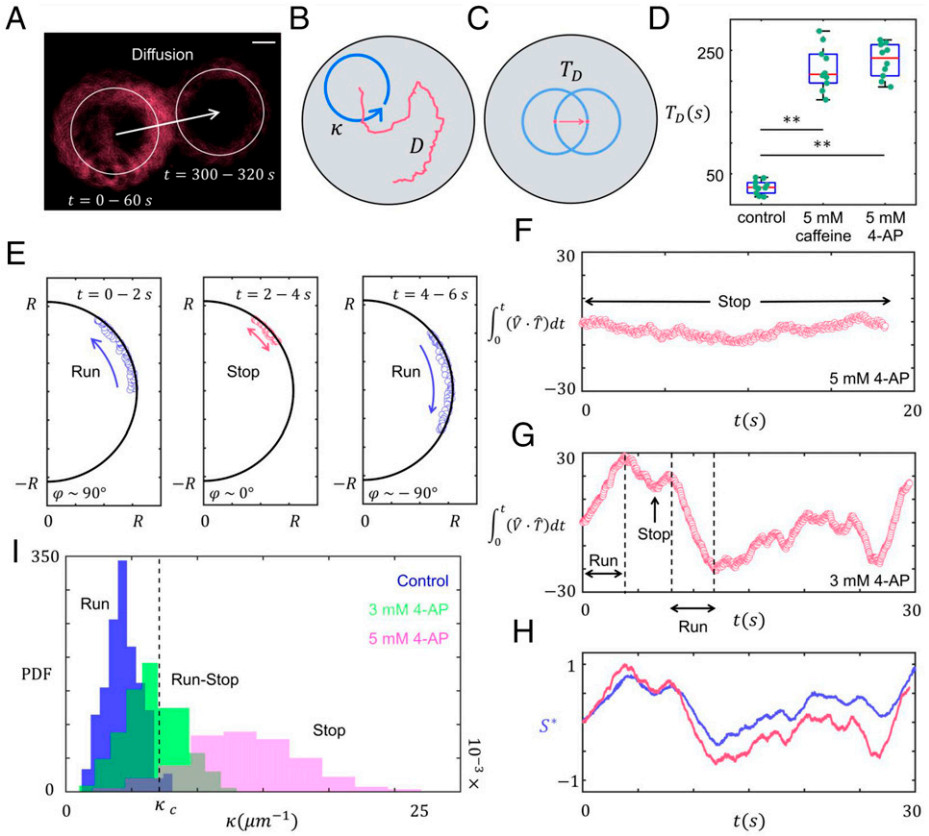

Fig. 4. Noise in the sperm intrinsic curvature. (*A*) Diffusivity of nonrolling sperm's circular motion caused by the noise in the intrinsic curvature. This image was obtained by combining frames taken from sperm circular motion at 50 frames/s. (Scale bar, 50 μm.) (*B* and *C*) Definition of κ, *D* and T_D. (*D*) T_D increased significantly with hyperactivation induced by 5 mM caffeine or 4-AP. **P value < 0.0001. These P values were obtained from two-tailed t tests, with adjustments for multiple comparisons (Bonferroni correction). (*E*) Sperm Run–Stop motion on the sidewall in a standard solution after treatment with 3 mM 4-AP, which incorporated change in the direction of swimming on the sidewall. Experimental measurements of sperm–sidewall orientation in Stop (5 mM 4-AP) (*F*) and Run–Stop (3 mM 4-AP) (*G*) types of motion. (*H*) Normalized sperm–sidewall orientation was proportional to the normalized arc length swum by sperm on the sidewall. (*I*) Probability density function of sperm intrinsic curvature with and without treatments. Noise promoted Run–Stop motion near the critical point.

sidewall after contacting it (Eq. **8** and *SI Appendix*, *Reciprocal Theorem and the Effect of Intrinsic Curvature* and *The Effect of Rolling*). Consequently, sperm average velocity on the sidewall is reduced to zero, as was also observed experimentally. We will refer to this behavior as "Stop" (Fig. 3*E*). In contrast, rolling sperm with $\kappa_{in} < \kappa_C$ swam along the sidewall after contacting it. We will refer to this behavior as "Run" (Fig. 3*E* and *SI Appendix*, *Sperm-Wall Interaction with and without Treatments*).

To characterize the transition from the isotropic Run motion on the sidewall that was observed in the absence of hyperactivation agonist to the Stop motion that was observed in most sperm treated with 5 mM of 4-AP or caffeine, we defined $Z = \hat{V} \cdot (\hat{N} + \hat{T})$ parameter. Note that $\hat{V}$ is a unit vector representing the sperm orientation on the sidewall, while $\hat{N}$ and $\hat{T}$ represent the normal and tangential directions of the sidewall at the contact point. Since Z is an average over the ensemble, it is equal to 0 when all sperm are exhibiting the Run motion isotropically on the sidewall, whereas $Z = 1$ corresponds to the situation in which all sperm exhibit Stop behavior on the sidewall (Fig. 3*F*). Experimental measurements of Z parameter at different concentrations of caffeine or 4-AP (Fig. 3*G*) indicate that transition from $Z = 0$ to $Z = 1$ obeys a logistic curve:

$$Z = \frac{1}{1 + e^{-\beta(c - c_o)}}, \qquad [9]$$

with $\beta = -1.01 \pm 0.38$ and $c_o = 2.22 \pm 0.48$ for 4-AP and $\beta = -1.09 \pm 0.21$ and $c_o = 2.07 \pm 0.46$ for caffeine. These values obtained from a linear regression model fitted to $\ln\left(\frac{1-Z}{Z}\right)$ using the least-squares approach.

Noise in the Sperm Intrinsic Curvature. Nonrolling sperm swim in circular paths, with curvature κ_{in} that depends on the level of asymmetry in the flagellar beating pattern. However, our measurements of the intrinsic curvature with and without the treatments indicated that it obeys a Gaussian distribution (Kolmogorov–Smirnov test) and thus may be simply written as $\kappa_{in}(t) = \kappa_{in} + \eta(t)$, where $\eta(t)$ is a delta-correlated, zero-mean white Gaussian noise. As a result of this noise in the intrinsic curvature and as our experimental measurements indicate, the center of the circular path diffuses in time (50) with diffusion coefficient D^s (Fig. 4*A* and Movies S8 and S9). Note that D^s is inversely correlated to the signal-to-noise ratio of the intrinsic curvature (*SI Appendix*, *Sperm Diffusive Circular Motion*). This diffusive circular motion that is observed in nonrolling sperm with and without agonist treatments is less susceptible to the sidewalls than are the movements of rolling sperm and becomes even less susceptible with hyperactivation. Therefore, this nonrolling circular motion could serve as a surface exploration mechanism through which the swimmer searches the top and bottom surfaces of the microfluidic reservoir enclosed by nearby physical side boundaries (Fig. 4*B*).

Our experimental measurements showed that with hyperactivation, the intrinsic curvature increased while the corresponding diffusion coefficients decreased significantly. As expected, nonrolling

hyperactivated sperm swept smaller areas than activated sperm. However, we were interested to know whether this decrease in the swept areas was solely due to the increase of the intrinsic curvature. To answer this question, we measured the characteristic time required for the center points of the sperm's circular paths to diffuse the corresponding radii $\left(T_D = \left(2D^s\ \kappa_{in}^2\right)^{-1}\right)$ with (control) and without 5 mM 4-AP or 5 mM caffeine treatments (Fig. 4*C*). Importantly, significant increase of T_D with agonist treatment (Fig. 4*D*) indicated that hyperactivation not only increases the curvature of paths but also results in relatively less noisy and more consistent pathways, which consequently yields decrease in the swept areas.

At 3 to 5 mM 4-AP (caffeine), we observed that 30.2±8.5% (26.2±11.3%), 10.8±2.4% (14.1±8.7%), and 3.5±1.0% (7.8±3.7%), respectively, of rolling sperm exhibited a "Run–Stop" motion on the sidewall. In this mixed type of motion, a sperm Run on the sidewall was interrupted by intermittent Stops. Remarkably, intermittent Stops could change the direction of swimming (Fig. 4*E*). To characterize this type of motion, we experimentally measured sperm orientation with respect to the sidewall $(\hat{V}\cdot\hat{T})$ for Stop (at 5 mM 4-AP; Fig. 4*F* and Movie S10) and Run–Stop (at 3 mM 4-AP; Fig. 4*G* and Movie S11) types of motion on the sidewall. Note that the change in the slope sign (Fig. 4*G*) indicates a change in the sperm swimming direction on the sidewall. Furthermore, we found that the normalized length swam by sperm on the wall (S^*) in the Run–Stop motion is correlated to the $\hat{V}\cdot\hat{T}$ (Fig. 4*H*).

To demonstrate that this Run–Stop behavior happens through increase of the intrinsic curvature above (or decay below) the critical point as well as the noise in the κ_{in} near the critical point, we measured sperm intrinsic curvature at 0, 3, and 5 mM of 4-AP, the distribution of which is shown in Fig. 4*I*. Since the intrinsic curvature obeys a Gaussian distribution $(\sim N(\kappa_{in},D))$ with the mean of κ_{in} and variance of D, the probabilities of sperm exhibiting Run (P_R) and Stop (P_S) and the phases of motion can be calculated as follows:

$$P_R(\kappa_{in}) = \int_0^{\kappa_c} N(\kappa_{in},D)d\kappa \approx \frac{1}{2}\left(1+\mathrm{erf}\left(\frac{\kappa_c-\kappa_{in}}{\sqrt{2D}}\right)\right),$$
$$P_S = 1-P_R. \qquad [10]$$

Note that the Gaussian noise in the intrinsic curvature is assumed to be delta correlated. Accordingly, the probability of transition between Run and Stop phases is:

$$P_{R\leftrightarrow S} = 2P_SP_R \approx \frac{1}{2}\left(1-\mathrm{erf}^2\left(\frac{\kappa_c-\kappa_{in}}{\sqrt{2D}}\right)\right). \qquad [11]$$

Eq. **11** indicates that the probability of sperm exhibiting transitions between Runs and Stops (Run–Stop phases) is maximum at $\kappa_{in}=\kappa_C$ and decays as κ_{in} moves away from the critical point. We measured P_R and $P_{R\leftrightarrow S}$ for distributions shown in Fig. 4*I* (using Eqs. **10** and **11**) and, in agreement with our observations, $P_R=0.99$ for nontreated sperm (Run), $P_R=0.59$ for sperm treated with 3 mM 4-AP (Run–Stop), and $P_R=0.09$ for sperm treated with 5 mM 4-AP (Stop). Furthermore, $P_{R\leftrightarrow S}=0.02$ for nontreated sperm, $P_{R\leftrightarrow S}=0.48$ for sperm treated with 3 mM 4-AP, and $P_{R\leftrightarrow S}=0.14$ for sperm treated with 5 mM 4-AP, which agrees with our observation that Run–Stop was observed mostly at 3 mM 4-AP (or caffeine) and therefore at an intermediate level of hyperactivation.

Note that at each transition from Stop to Run, sperm may change the direction of swimming depending on the sign of $\Delta\kappa$ at the time of transition. Assuming that the probability of change in the swimming direction after each Stop to Run transition is $\frac{1}{2}$, this Run–Stop type of motion can be modeled by a one-dimensional Markovian random walk (51), with effective diffusion coefficient of the following:

$$D_{\mathrm{eff}}^{\mathrm{Run-Stop}} = \frac{1}{2}V_p^2\tau\cdot\left(\frac{P_R}{P_S}\right). \qquad [12]$$

Note that τ refers to the time of sperm rotation from $\varphi=0$ to $\varphi=\pm\frac{\pi}{2}$ and thus the transition from Stop to Run (*SI Appendix*, *Sperm Run-Stop Motion on the Sidewall*). While experimentally measuring $D_{\mathrm{eff}}^{\mathrm{Run-Stop}}$ for sperm performing Run–Stop motion at 3 to 4 mM 4-AP, we noticed that the effective diffusion coefficient decreased with concentration (*SI Appendix*, *Experimental Measurements of* $D_{eff}^{Run-Stop}$). The results that we presented in this part reveal that while the implications of noise in the sperm's intrinsic curvature are negligible without agonist, upon hyperactivation, noise promotes new swimming behaviors on the sidewall.

Sperm Pseudo-Chemotaxis. The concentration-dependent modulation of sperm intrinsic curvature and thus sidewall interactions by agonists that induce hyperactivation in vitro indicates that in vivo sperm guidance by walls is regulated by biochemical stimuli. One aspect of this important phenomenon became apparent when we investigated sperm movement between two connected reservoirs (Fig. 5*A*), one of which (the source) was filled with control TALP solution and the other (the sink) was filled with 0, 3, or 5 mM 4-AP or caffeine in TALP. Note that there was negligible fluid flow introduced into the device at the time of the experiments. All sperm cells were initially within the source reservoir, and as time proceeded, we observed sperm migration from the source to the sink. After 5 min, we gently washed the source with control TALP and counted the number of sperm that exited the sink reservoir (n_{out}).

Calculating $N_{out}=\int n_{out}dt$, we noticed that, with no caffeine or 4-AP in the sink, more than 98.0 ± 1.0% of sperm evacuated the sink and returned to the source in 58.2 ± 3 s. However, as we increased the concentration of caffeine in the sink to 3 mM and 5 mM, only 44.2 ± 4.3% and 12.4 ± 3.7% of sperm left the sink and returned to the source in 60 s (Fig. 5*B*). These numbers for 3 mM and 5 mM of 4-AP in the sink were 24.1 ± 3.4% and 5.7 ± 1.3% in 60 s, respectively (Fig. 5*D*). These fractions increased to 53.0 ± 6.3% (3 mM caffeine), 14.8 ± 2.1% (5 mM caffeine), 35.3 ± 8.1% (3 mM 4-AP), and 6.2 ± 1.4% (5 mM 4-AP) after 120 s (*SI Appendix*, Table S1 in *SI Appendix*, *Sperm Pseudo-chemotaxis*). To ensure that these results were solely caused by agonist treatments in the sink rather than other potential factors, we set the agonist concentration equal to 0 in the sink and added caffeine or 4-AP to the source. The source treatments were 3 or 5 mM of caffeine or 4-AP. Our results (*SI Appendix*, *Sperm Pseudo-chemotaxis*) indicate that these treatments did not influence sink evacuation time and sperm return to the source in 64.7 ± 3.8 s.

We call this behavior "pseudo-chemotaxis" as it enables sperm to accumulate within reservoirs with higher concentrations of hyperactivation agonists. We stress that pseudo-chemotaxis is not a drift motion toward a region with higher concentrations of chemical stimuli, which was reported previously for sperm of sea urchin and known as chemotaxis (52, 53). Pseudo-chemotactic behavior in standard solution is caused by two effects of hyperactivation: 1) hyperactivation decreases sperm average path velocity (V_{AP}) prior to sidewall contact and 2) hyperactivation increases sperm intrinsic curvature above the critical value, which reduces sperm motion on the sidewall, as described in Figs. 3 and 4. In fact, V_{AP} of sperm without treatment is higher than that of sperm treated with caffeine or 4-AP, which results in a subsequent increase of the sperm residence time within reservoirs with higher concentrations of caffeine or 4-AP. Furthermore, V_{AP} of a sperm without treatment drops to zero upon contact with the sidewall and, in less than 1 s, returns to the initial V_{AP} (before contact) and swims along the sidewall until it exits the sink. However, V_{AP} of

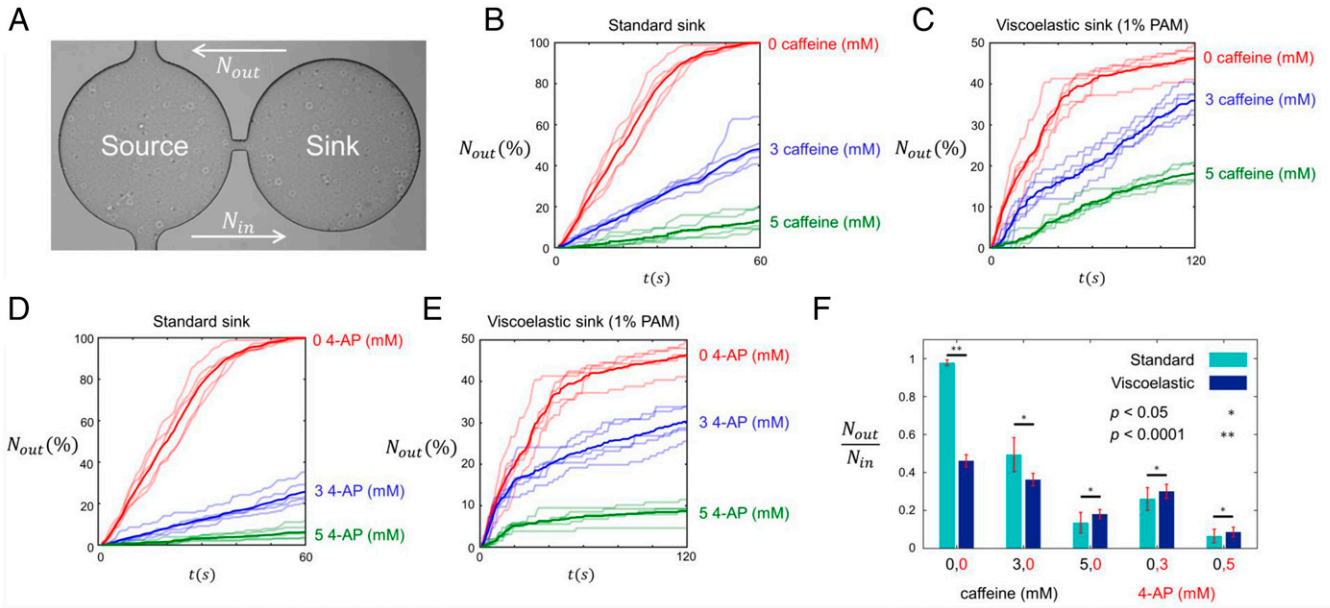

Fig. 5. Sperm pseudo-chemotaxis. (*A*) Two circular reservoirs (diameter: 600 μm) connected by a narrow channel (width: 40 μm). The left reservoir (Source) is filled with standard solution and no agonist; the right (Sink) contains treatments. Viscoelastic sinks contained 1% PAM. N_{out} as the cumulative percentage of sperm that exited the standard (*B*) and viscoelastic (*C*) sinks at 0, 3, and 5 mM caffeine. N_{out} as the cumulative percentage of sperm that exited the standard (*D*) and viscoelastic (*E*) sinks at 0, 3, and 5 mM 4-AP. All transparent lines indicate replicates, while the lines with solid colors indicate the means. (*F*) $^{N_{out}}/_{N_{in}}$ ratios, corresponding to viscoelastic and standard sinks with different concentrations of caffeine or 4-AP. The *P* values were obtained from two-tailed *t* tests.

a single sperm treated with 5 mM of 4-AP (or caffeine) drops to zero upon contact and does not return to the initial V_{AP} (*SI Appendix*, *Sperm Pseudo-chemotaxis*). Therefore, the decrease in sperm average path velocity as well as the negligible guiding effect of sidewalls on hyperactivated sperm contribute to the observed pseudo-chemotactic behavior.

Similar observations were made when we added 1% PAM to increase viscoelasticity in the sink to mimic the effect of mucus in areas of the female reproductive tract (Fig. 5 *C* and *E*). At 0 mM caffeine or 4-AP in the viscoelastic sink, 46.5 ± 8.7% of sperm returned to the source after 120 s, and this number reached a plateau of 61.6 ± 8.3% after 300 s. As we increased the concentration of caffeine to 3 mM and 5 mM, 36.8 ± 3.4% and 17.2 ± 2.6% returned to the source after 120 s. These numbers increased to 53.0 ± 8.5% and 22.4 ± 5.0% after 300 s. When we used 3 mM and 5 mM of 4-AP instead of caffeine, 30.0 ± 4.3% (39.1 ± 8.7%) and 8.2 ± 3.4% (9.4 ± 4.7%) of sperm returned to the source after 120 s (300 s) (*SI Appendix*, Table S1 in *SI Appendix*, *Sperm Pseudo-chemotaxis*).

This pseudo-chemotactic behavior in viscoelastic solution is caused by two other effects of hyperactivation: 1) hyperactivation increases the characteristic time of the diffusive circular motion of sperm and 2) hyperactivation increases sperm intrinsic curvature above the critical value, which reduces sidewall interactions. In fact, the increase in the characteristic time of the diffusive circular motion implies that the center of the circular path diffuses more slowly, which subsequently increases sperm residence time in the reservoirs with higher concentrations of agonists. Furthermore, the increase of sperm intrinsic curvature above the critical value during hyperactivation transitions sidewall interactions from Categories 1, 2, and 3 to Category 4 and thus reduces sperm guidance via sidewall interactions, even close to the sidewall. To support this claim, we calculated the portion of sperm that evacuated the viscoelastic sink by swimming along the sidewall in the viscoelastic solution at different concentrations of agonists and noticed that more than ~90% of sperm evacuated the viscoelastic sink via sidewall interactions (*SI Appendix*, *Sperm Pseudo-chemotaxis*). That is, the transition of sidewall interactions from Categories 1, 2, and 3 to Category 4, which occurs through hyperactivation, directly contributes to the observed pseudo-chemotactic behavior.

These percentages, obtained from sperm return to the source after entry to the sink, indicate that difference in the viscoelasticity as well as difference in the concentration of hyperactivation-inducing agonists directly influence sperm movement between two connected reservoirs and could do so for similarly connected regions in the female tract. Based on the numbers obtained for N_{in} and N_{out} after 120 s, we calculated $^{N_{out}}/_{N_{in}}$, which represents the portion of sperm that exited from the standard and viscoelastic sinks after agonist treatments and returned to the source (Fig. 5*F*). While comparing the values obtained for $^{N_{out}}/_{N_{in}}$, one notices that this fraction decreases with increase of the agonist concentration in the sink for both standard and viscoelastic solutions. A more interesting conclusion was obtained when we compared this fraction between standard and viscoelastic solutions with identical agonist concentrations. In controls, this fraction for the viscoelastic sink (0.44 ± 0.06) was much lower (P value < 0.0001) than that from the standard sink (0.99 ± 0.01), meaning that, in the absence of chemical stimuli, the difference between viscoelasticity of the source and the sink highly influences sperm migration between two reservoirs. As the concentration of caffeine or 4-AP increased to 3 mM, the difference between $^{N_{out}}/_{N_{in}}$ for viscoelastic and standard sinks decayed. Eventually, for 5 mM of caffeine or 4-AP, the difference between $^{N_{out}}/_{N_{in}}$ for viscoelastic and standard sinks decayed to a negligible degree. The decay in the difference between $^{N_{out}}/_{N_{in}}$ for viscoelastic and standard sinks with the agonist treatments implies that the biochemical factors contributed more strongly to sperm movement between the two reservoirs than did the viscoelasticity difference between the reservoirs.

Progesterone Induces Similar Responses in Bovine Sperm. Although the pharmacological agonists for mammalian sperm hyperactivation (25–27, 36, 38, 54) have been well established, physiological

agonists that induce hyperactivation in vivo have not yet been firmly established. Nevertheless, progesterone (P4) has recently been reported to induce hyperactivation in frozen/thawed bull sperm (55), so we tested P4 to determine whether it induces the same hyperactivation swimming patterns that we observed for caffeine and 4-AP. To measure the percentage of hyperactivated sperm after each treatment, we set a quantitative definition of hyperactivation and identified sperm with $\varphi < 60^{\circ}$ as hyperactivated. Note that for a full Stop, $\varphi \sim 0^{\circ}-15^{\circ}$, and for a full Run, $\varphi \sim 70^{\circ}-90$. We found that treatment with 10, 50, and 250 nM P4 resulted in 42±5% (total count = 50, 48, and 51), 45±2% (total count = 67, 52, and 68), and 41±8% (total count = 42, 41, 35) hyperactivation, respectively, which differed significantly from the control ($P < 0.001$, t tests with Bonferroni corrections). We also observed transition from Run to Stop on the sidewall in sperm hyperactivated with P4, and the measured Z parameter increased accordingly with P4 treatments (*SI Appendix*, *The Effect of Progesterone*). It should be noted that our microfluidics devices were constructed using polydimethylsiloxane (PDMS), currently the most widely used polymer for biomicrofluidic devices, because it is transparent, flexible, binds strongly to glass slides, and is permeable to oxygen (56). PDMS has been found to absorb steroids like P4 (56, 57), and therefore, the concentration of P4 available to the sperm throughout the experiment may have varied. Further studies using other construction materials for devices, such as agarose (58), are warranted.

Discussion

To summarize, our results revealed the effects of hyperactivation on sperm–sidewall interactions. We found that sperm undergoing hyperactivation exhibited higher intrinsic curvature, depending on the concentration of the hyperactivating agonist, while the rate of rolling remained unaffected. Remarkably, we found that the transformation of motility by hyperactivation diminished the guiding influence of sidewalls on sperm movement when the intrinsic curvature of sperm exceeded a critical value. We further found that the reduction of the influence of sidewalls on sperm movement resulted in a pseudo-chemotactic behavior through which sperm accumulated within reservoirs with higher concentrations of hyperactivating agonist. We called this phenomenon "pseudo-chemotaxis," because it was mainly due to an increase of sperm residence time in reservoirs with higher agonist concentrations rather than to a deterministic drift of sperm toward higher concentrations.

Since the intrinsic curvature exhibited nonthermal Gaussian noise, we also investigated the effect of this noise on sperm motion and subsequent sidewall interactions. Considering that the noise in the intrinsic curvature produced a diffusive component into the circular motion of nonrolling sperm, we found that the diffusivity and the characteristic time of the circular motion decreased significantly with hyperactivation, and circular motion exhibited more consistency. Moreover, noise in the intrinsic curvature of rolling sperm (standard solution) near the critical value resulted in a remarkable Run–Stop motion along the sidewall. This Run–Stop motion is a one-dimensional Markovian random walk that incorporates changes into the swimming direction of sperm on the sidewall.

Our results are obtained from investigating sperm motion within high-aspect, circular microfluidic reservoirs. These reservoirs are designed to be high aspect ratio so that they mimic narrow channels in surfaces and narrow spaces between mucosal folds (*SI Appendix*, *Materials and Methods*) within the female reproductive tract. Although the circular and smooth shape of the sidewalls of reservoirs might not fully represent the sidewalls of the female reproductive tract, this specific geometry was chosen to minimize the influence of geometrical features such as corners and curvature gradients on sperm motion. That is, our results are solely due to the effect of hyperactivation on sperm–sidewall interactions rather than other potential factors.

The biochemical factor(s) that trigger hyperactivation in vivo have not been firmly established and various factors may trigger hyperactivation at different functional regions within the female reproductive tract. Furthermore, the signaling pathway involved in the induction of hyperactivation in vitro depends on the biochemicals used for such a purpose. For instance, caffeine, as one of the hyperactivation-inducing agonists used in this study, activates CATSPER channels and elevates the cytoplasmic Ca^{2+} concentration by influx of exogenous Ca^{2+} (59). There is evidence that caffeine cannot induce hyperactivation in Ca^{2+}-depleted medium (32). In contrast, there is evidence that 4-AP induces hyperactivation by mobilizing intracellular stored Ca^{2+} as well as by activating CATSPER channels, and accordingly, 4-AP can induce hyperactivation in Ca^{2+}-depleted medium (60). Our use of caffeine and 4-AP as commonly used agonists with different mechanisms for induction of hyperactivation and yet obtaining quantitatively similar outcomes suggests that our results stand independent of the factors that trigger hyperactivation. Therefore, these results are likely to be broadly applicable to the other agonists of hyperactivation, particularly the factors that induce hyperactivation in vivo.

Previous studies suggested that hyperactivation occurs first in the oviduct, as hyperactivated sperm have not been observed to pass through the uterotubal junction (61). If this is true, the Run phase of motion on the wall may contribute to sperm navigation within the lower part of the female reproductive tract and before reaching the oviduct. Low concentrations of the biochemical factor(s) that trigger hyperactivation did not eliminate the Run mode, thereby allowing wall-determined navigation to continue to function. However, once the concentration rose to a critical threshold that corresponded to the critical intrinsic curvature, rolling sperm would exhibit Run–Stop motion on the sidewalls of the female reproductive tract. This motion might be the sperm navigational mechanism at intermediate distances from a source of agonists or at a low concentration of agonists in vivo. Eventually, once the concentration exceeded the critical threshold by some amount, navigation along walls would be diminished, and the sperm would Stop on its position on the wall.

In regions within the female reproductive tract where fluid viscoelasticity is high, rolling would be suppressed. Based on our results, we anticipate that the motion of sperm in these regions would be diffusive and circular, so that radii, sidewall interactions, and diffusion coefficients would decrease with hyperactivation. That is, as sperm swim in higher concentrations of hyperactivation agonists, they would perform tighter and more consistent circular motions, which are not susceptible to nearby sidewalls.

Modulation of sperm motility via hyperactivation results in pseudo-chemotactic behavior, through which sperm accumulate within reservoirs with higher concentrations of hyperactivation agonists. In contrast to the chemotaxis observed in sperm of sea urchins, this pseudo-chemotactic behavior is due to the increase of sperm residence time in regions with higher concentrations rather than to a deterministic drift of sperm toward higher concentrations of biochemical stimuli (53). This behavior suggests that as sperm ascend the female reproductive tract and move into regions with high concentrations of hyperactivation-inducing factors, they become less likely to leave those regions and return to the regions with lower concentrations.

Our results reveal the potential role of hyperactivation in mammalian sperm navigation within the female reproductive tract. Our findings demonstrate that hyperactivation regulates sperm–sidewall interactions and navigation via physical boundaries, which suggests that a combination of biochemical and

biophysical cues organizes sperm navigation within the confined and complex environment of the female reproductive tract. Furthermore, since hyperactivation occurs in the oviduct far from the oocyte and even before ovulation, most likely through biochemicals secreted from the female reproductive tract (62–64), our results suggest that the contribution of biochemical factors to sperm navigation may not be limited to chemotaxis at close distances from the oocyte, and they modulate sperm navigation even at far and intermediate distances from the oocyte.

Materials and Methods

Sperm Preparation and Chemicals. Commercially available cryopreserved semen of *Bos taurus* (5.5 to 6.5 y of age) diluted in egg yolk extender were generously donated by GENEX under the URUS holding company, Ithaca. The ejaculate concentration was 50×10^6 sperm per straw (0.25 mL) with prefreeze motility of 65%. A combination of gentamicin, tylosin, lincomycin, and spectinomycin were added to the semen as antibiotics prior to cryopreservation. For each experiment, two straws were thawed in a 38 °C water bath for 30 s and then diluted with 1 mL TALP (36). The sperm samples and microfluidic device were maintained at 38 °C throughout the experiments using a heated glass microscope plate (Bioscience tools).

All chemicals used for this study were purchased from Sigma-Aldrich, unless specified. TALP medium contained the following: NaCl (110 mM), KCl (2.68 mM), NaH_2PO_4 (0.36 mM), $NaHCO_3$ (25 mM), $MgCl_2$ (0.49 mM), $CaCl_2$ (2.4 mM), Hepes buffer (25 mM), glucose (5.56 mM), pyruvic acid (1.0 mM), penicillin G (0.006% or 3 mg/500 mL), and bovine serum albumin (20 mg/mL, Caisson Labs). After preparation, the pH of the medium was adjusted to 7.3 to 7.4 by gradual addition of HCl. We did not observe significant change in the pH after addition of caffeine and 4-AP to the medium.

To tether the sperm head to the glass surface, we reduced the concentration of bovine serum albumin to 5 mg/mL (43). To increase the viscoelasticity of TALP to suppress sperm rolling, we added 1% (by weight) long-chain PAM with molecular weight of ~5 to 6 MDa (39). The rheological properties of the standard and viscoelastic solutions were measured by a TA Instruments HR-3 Rheometer available at Cornell Center for Material Research. To induce hyperactivation, various concentrations of caffeine and 4-AP (Santa Cruz Biotechnology), as commonly used hyperactivation-inducing pharmacological agonists, were added to the TALP solution.

Microfabrication and Microscopy. Our microfluidic device (*SI Appendix, Materials and Methods*) was made of PDMS through a standard soft lithography protocol available at Cornell NanoScale Facility (65). The height of the microfluidic device was 30 μm, and the diameter of the circular reservoirs was 600 μm. After injecting the culture medium and pharmacological agonists used in this paper into the reservoirs and degassing, diluted sperm samples were injected into the microfluidic device using gravity. The flow generated in the channel was controlled by changing the height of the semen container. This method enabled us to decrease the injection rate and increase the rate of sperm entry into the reservoirs. Sperm motion within the reservoirs was observed with a Nikon Eclipse TE300 inverted phase-contrast microscope (20× and 40× magnifications) and recorded with an Andor Zyla 5.5s camera (25 and 50 frames/s). Sperm rolling under the phase contract optics was identified through change in the sperm head light intensity (12, 42).

Cell Tracking. To extract sperm trajectories, we used both manual and automatic head tracking depending on the resolution of our acquired videos. Our automatic tracking method was based on tracking a single sperm using image subtraction and tracking the centroid of the moving element identified with Farneback method (66). Overlaying consecutive frames acquired at 0.08-s intervals from moving sperm yielded sperm trajectories. To characterize the midpiece bending, we removed Gaussian noise and background image using a simple Gaussian filter and image subtraction. We then binarized the images acquired at 25 frames/s into black and white and measured the deviation of the midpiece (or alternatively sperm head) from the centerline. Fast Fourier transform of the extracted signal demonstrated that the zeroth harmonic of the signal is related to the tethered sperm angular velocity, which increased with hyperactivation. This method was based on previously established reports, and the findings are in agreement with the literature on the asymmetry in the sperm flagellar beating (40). To measure the angle between sperm and the wall, we used manual measurements as well as the "Eccentricity" and "Orientation" properties of "regionprops" command in MATLAB, depending on the quality of the videos and number of sperm within the field of interest.

Numerical Simulation. The following numerical simulation is based on previous numerical and experimental studies on the hydrodynamic interaction of sperm (or bacteria) with a flat surface (46). To simulate sperm–sidewall interactions, we modeled sperm as a high–aspect ratio rod (10:1) and used a finite element method to solve Stokes and mass conservation equations (COMSOL MULTIPHYSICS) at the lubrication limit (67). The corresponding boundary conditions were $u = V_p$ on sperm surface and $u = 0$ on the sidewall. To calculate the angular velocity imposed on the sperm by the sidewall, we extracted the pressure exerted on the sperm (p) at varying incident angles for a range of constant progressive velocities ($V_p = 40 - 80\ \mu m/s$) and calculated the toque acted upon sperm by pressure. Applying torque-free constraint, the toque produced by pressure was canceled out with the torque produced by drag force, and consequently, sperm angular velocity (Ω_w) was then calculated using Eq. **13**:

$$\Omega_w(\varphi) = \frac{\int_0^l (x - x_{CM}) p(x, \varphi) dx}{\left(\frac{\xi_N}{\lambda}\right) \int_0^l (x - x_{CM})^2 dx}. \quad [13]$$

Note that x-axis is set parallel to the long axis of the rod with $x = 0$ at the sidewall contact point (Fig. 2*B*), x_{cm} is the coordinate of the sperm center of mass on x-axis, l is the sperm length, ξ_N is the drag coefficient in normal direction, and λ is a fitting parameter equal to 1.5×10^{-3}. This fitting parameter is needed because the experimental value reported for ξ_N (40) corresponds to a three-dimensional motion, while our model is two-dimensional. In agreement with previous studies (46), our simulations indicate that p is linearly proportional to the V_p, so we define a function $g(\varphi)$ (Eq. **14**) that is independent of propulsive velocity and describes the dynamic of sperm–sidewall interactions:

$$g(\varphi) = \frac{\lambda}{V_p \cdot \xi_N} \frac{\int_0^l (x - x_{CM}) p(x, \varphi) dx}{\int_0^l (x - x_{CM})^2 dx}. \quad [14]$$

For full derivations of Eqs. **13** and **14**, refer to *SI Appendix, Sperm-Wall Interaction after Contact*. We also provide a table of parameters in *SI Appendix*.

Data Availability. All study data are included in the article and/or supporting information. Additional data have been deposited in Figshare (https://figshare.com/projects/Mammalian_sperm_hyperactivation_regulates_navigation_via_physical_boundaries_and_promotes_pseudo-chemotaxis/124672).

ACKNOWLEDGMENTS. We thank C.K. Tung and D. Koch for helpful discussions on sperm–wall hydrodynamic interactions. We also thank H. Florman for helpful discussion on bovine sperm hyperactivation induced by P4 treatments. We also thank K.J. Donaghy for helping us edit this manuscript. This work was performed in part at the Cornell NanoScale Facility, a member of the National Nanotechnology Coordinated Infrastructure, which is supported by the NSF (Grant ECCS-1542081).

1. M. Eisenbach, L. C. Giojalas, Sperm guidance in mammals—An unpaved road to the egg. *Nat. Rev. Mol. Cell Biol.* **7**, 276–285 (2006).
2. S. S. Suarez, A. A. Pacey, Sperm transport in the female reproductive tract. *Hum. Reprod. Update* **12**, 23–37 (2006).
3. K. Miki, D. E. Clapham, Rheotaxis guides mammalian sperm. *Curr. Biol.* **23**, 443–452 (2013).
4. C. K. Tung *et al.*, Microgrooves and fluid flows provide preferential passageways for sperm over pathogen *Tritrichomonas foetus*. *Proc. Natl. Acad. Sci. U.S.A.* **112**, 5431–5436 (2015).
5. V. Kantsler, J. Dunkel, M. Blayney, R. E. Goldstein, Rheotaxis facilitates upstream navigation of mammalian sperm cells. *eLife* **3**, e02403 (2014).
6. A. Bukatin, I. Kukhtevich, N. Stoop, J. Dunkel, V. Kantsler, Bimodal rheotactic behavior reflects flagellar beat asymmetry in human sperm cells. *Proc. Natl. Acad. Sci. U.S.A.* **112**, 15904–15909 (2015).
7. M. Zaferani, S. H. Cheong, A. Abbaspourrad, Rheotaxis-based separation of sperm with progressive motility using a microfluidic corral system. *Proc. Natl. Acad. Sci. U.S.A.* **115**, 8272–8277 (2018).
8. P. Denissenko, V. Kantsler, D. J. Smith, J. Kirkman-Brown, Human spermatozoa migration in microchannels reveals boundary-following navigation. *Proc. Natl. Acad. Sci. U.S.A.* **109**, 8007–8010 (2012).
9. R. Nosrati, A. Driouchi, C. M. Yip, D. Sinton, Two-dimensional slither swimming of sperm within a micrometre of a surface. *Nat. Commun.* **6**, 8703 (2015).
10. V. Kantsler, J. Dunkel, M. Polin, R. E. Goldstein, Ciliary contact interactions dominate surface scattering of swimming eukaryotes. *Proc. Natl. Acad. Sci. U.S.A.* **110**, 1187–1192 (2013).
11. A. Guidobaldi *et al.*, Geometrical guidance and trapping transition of human sperm cells. *Phys. Rev. E Stat. Nonlin. Soft Matter Phys.* **89**, 032720 (2014).

12. M. Zaferani, G. D. Palermo, A. Abbaspourrad, Strictures of a microchannel impose fierce competition to select for highly motile sperm. *Sci. Adv.* **5**, eaav2111 (2019).
13. M. Zaferani, F. Javi, A. Mokhtare, P. Li, A. Abbaspourrad, Rolling controls sperm navigation in response to the dynamic rheological properties of the environment. *eLife* **10**, e68693 (2021).
14. A. Bahat *et al.*, Thermotaxis of mammalian sperm cells: A potential navigation mechanism in the female genital tract. *Nat. Med.* **9**, 149–150 (2003).
15. A. Bahat, M. Eisenbach, Sperm thermotaxis. *Mol. Cell. Endocrinol.* **252**, 115–119 (2006).
16. H. Chang, S. S. Suarez, Rethinking the relationship between hyperactivation and chemotaxis in mammalian sperm. *Biol. Reprod.* **83**, 507–513 (2010).
17. D. Ralt *et al.*, Sperm attraction to a follicular factor(s) correlates with human egg fertilizability. *Proc. Natl. Acad. Sci. U.S.A.* **88**, 2840–2844 (1991).
18. F. Sun *et al.*, Human sperm chemotaxis: Both the oocyte and its surrounding cumulus cells secrete sperm chemoattractants. *Hum. Reprod.* **20**, 761–767 (2005).
19. L. Armon, M. Eisenbach, Behavioral mechanism during human sperm chemotaxis: Involvement of hyperactivation. *PLoS One* **6**, e28359 (2011).
20. R. Yanagimachi, The movement of golden hamster spermatozoa before and after capacitation. *J. Reprod. Fertil.* **23**, 193–196 (1970).
21. S. S. Suarez, Control of hyperactivation in sperm. *Hum. Reprod. Update* **14**, 647–657 (2008).
22. S. S. Suarez, Mammalian sperm interactions with the female reproductive tract. *Cell Tissue Res.* **363**, 185–194 (2016).
23. S. S. Suarez, I. Revah, M. Lo, S. Kölle, Bull sperm binding to oviductal epithelium is mediated by a Ca2+-dependent lectin on sperm that recognizes Lewis-a trisaccharide. *Biol. Reprod.* **59**, 39–44 (1998).
24. D. J. Miller, Regulation of sperm function by oviduct fluid and the epithelium: Insight into the role of glycans. *Reprod. Domest. Anim.* **50** (suppl. 2), 31–39 (2015).
25. B. Marquez, S. S. Suarez, Different signaling pathways in bovine sperm regulate capacitation and hyperactivation. *Biol. Reprod.* **70**, 1626–1633 (2004).
26. B. Marquez, S. S. Suarez, Bovine sperm hyperactivation is promoted by alkaline-stimulated Ca2+ influx. *Biol. Reprod.* **76**, 660–665 (2007).
27. H.-C. Ho, K. A. Granish, S. S. Suarez, Hyperactivated motility of bull sperm is triggered at the axoneme by Ca2+ and not cAMP. *Dev. Biol.* **250**, 208–217 (2002).
28. P. V. Lishko *et al.*, The control of male fertility by spermatozoan ion channels. *Annu. Rev. Physiol.* **74**, 453–475 (2012).
29. H. Wang, L. L. McGoldrick, J.-J. Chung, Sperm ion channels and transporters in male fertility and infertility. *Nat. Rev. Urol.* **18**, 46–66 (2021).
30. B. Marquez, G. Ignotz, S. S. Suarez, Contributions of extracellular and intracellular Ca2+ to regulation of sperm motility: Release of intracellular stores can hyperactivate CatSper1 and CatSper2 null sperm. *Dev. Biol.* **303**, 214–221 (2007).
31. S. Costello *et al.*, Ca2+-stores in sperm: Their identities and functions. *Reproduction* **138**, 425–437 (2009).
32. H.-C. Ho, S. S. Suarez, An inositol 1,4,5-trisphosphate receptor-gated intracellular Ca(2+) store is involved in regulating sperm hyperactivated motility. *Biol. Reprod.* **65**, 1606–1615 (2001).
33. T. A. Quill *et al.*, Hyperactivated sperm motility driven by CatSper2 is required for fertilization. *Proc. Natl. Acad. Sci. U.S.A.* **100**, 14869–14874 (2003).
34. H. Qi *et al.*, All four CatSper ion channel proteins are required for male fertility and sperm cell hyperactivated motility. *Proc. Natl. Acad. Sci. U.S.A.* **104**, 1219–1223 (2007).
35. S. S. Suarez, X. Dai, Hyperactivation enhances mouse sperm capacity for penetrating viscoelastic media. *Biol. Reprod.* **46**, 686–691 (1992).
36. F. Ardon *et al.*, Dynamics of bovine sperm interaction with epithelium differ between oviductal isthmus and ampulla. *Biol. Reprod.* **95**, 90–91 (2016).
37. E. H. Ooi, D. J. Smith, H. Gadêlha, E. A. Gaffney, J. Kirkman-Brown, The mechanics of hyperactivation in adhered human sperm. *R. Soc. Open Sci.* **1**, 140230 (2014).
38. G. G. Ignotz, S. S. Suarez, Calcium/calmodulin and calmodulin kinase II stimulate hyperactivation in demembranated bovine sperm. *Biol. Reprod.* **73**, 519–526 (2005).
39. C. K. Tung *et al.*, Fluid viscoelasticity promotes collective swimming of sperm. *Sci. Rep.* **7**, 3152 (2017).
40. B. M. Friedrich, I. H. Riedel-Kruse, J. Howard, F. Jülicher, High-precision tracking of sperm swimming fine structure provides strong test of resistive force theory. *J. Exp. Biol.* **213**, 1226–1234 (2010).
41. S. Gadadhar, *et al.*, Tubulin glycylation controls axonemal dynein activity, flagellar beat, and male fertility. *Science* **371**, eabd4914 (2021).
42. C. K. Tung *et al.*, Emergence of upstream swimming via a hydrodynamic transition. *Phys. Rev. Lett.* **114**, 108102 (2015).
43. G. Saggiorato *et al.*, Human sperm steer with second harmonics of the flagellar beat. *Nat. Commun.* **8**, 1415 (2017).
44. J. Elgeti, R. G. Winkler, G. Gompper, Physics of microswimmers—Single particle motion and collective behavior: A review. *Rep. Prog. Phys.* **78**, 056601 (2015).
45. J. Elgeti, G. Gompper, Microswimmers near surfaces. *Eur. Phys. J. Spec. Top.* **225**, 2333–2352 (2016).
46. G. Li, J. X. Tang, Accumulation of microswimmers near a surface mediated by collision and rotational Brownian motion. *Phys. Rev. Lett.* **103**, 078101 (2009).
47. O. Sipos, K. Nagy, R. Di Leonardo, P. Galajda, Hydrodynamic trapping of swimming bacteria by convex walls. *Phys. Rev. Lett.* **114**, 258104 (2015).
48. R. Nosrati, P. J. Graham, Q. Liu, D. Sinton, Predominance of sperm motion in corners. *Sci. Rep.* **6**, 26669 (2016).
49. T. Ostapenko *et al.*, Curvature-guided motility of microalgae in geometric confinement. *Phys. Rev. Lett.* **120**, 068002 (2018).
50. R. Ma, G. S. Klindt, I. H. Riedel-Kruse, F. Jülicher, B. M. Friedrich, Active phase and amplitude fluctuations of flagellar beating. *Phys. Rev. Lett.* **113**, 048101 (2014).
51. H. C. Berg, *Random Walks in Biology* (Princeton University Press, 1993).
52. J. F. Jikeli *et al.*, Sperm navigation along helical paths in 3D chemoattractant landscapes. *Nat. Commun.* **6**, 7985 (2015).
53. B. M. Friedrich, F. Jülicher, Chemotaxis of sperm cells. *Proc. Natl. Acad. Sci. U.S.A.* **104**, 13256–13261 (2007).
54. I. A. H. Barakat, M. A. Danfour, F. A. M. Galewan, M. A. Dkhil, Effect of various concentrations of caffeine, pentoxifylline, and kallikrein on hyperactivation of frozen bovine semen. *BioMed Res. Int.* **2015**, 948575 (2015).
55. J. Romero-Aguirregomezcorta, S. Cronin, E. Donnellan, S. Fair, Progesterone induces the release of bull spermatozoa from oviductal epithelial cells. *Reprod. Fertil. Dev.* **31**, 1463–1472 (2019).
56. K. J. Regehr *et al.*, Biological implications of polydimethylsiloxane-based microfluidic cell culture. *Lab Chip* **9**, 2132–2139 (2009).
57. M. W. Toepke, D. J. Beebe, PDMS absorption of small molecules and consequences in microfluidic applications. *Lab Chip* **6**, 1484–1486 (2006).
58. H. Chang, B. J. Kim, Y. S. Kim, S. S. Suarez, M. Wu, Different migration patterns of sea urchin and mouse sperm revealed by a microfluidic chemotaxis device. *PLoS One* **8**, e60587 (2013).
59. G. P. Johnson *et al.*, Genomic identification, expression profiling, and functional characterization of CatSper channels in the bovine. *Biol. Reprod.* **97**, 302–312 (2017).
60. W. Alasmari *et al.*, Ca2+ signals generated by CatSper and Ca2+ stores regulate different behaviors in human sperm. *J. Biol. Chem.* **288**, 6248–6258 (2013).
61. P. Gaddum-Rosse, Some observations on sperm transport through the uterotubal junction of the rat. *Am. J. Anat.* **160**, 333–341 (1981).
62. G. W. Cooper, J. W. Overstreet, D. F. Katz, The motility of rabbit spermatozoa recovered from the female reproductive tract. *Gamete Res.* **2**, 35–42 (1979).
63. J. W. Overstreet, G. W. Cooper, Effect of ovulation and sperm motility on the migration of rabbit spermatozoa to the site of fertilization. *J. Reprod. Fertil.* **55**, 53–59 (1979).
64. S. S. Suárez, R. A. Osman, Initiation of hyperactivated flagellar bending in mouse sperm within the female reproductive tract. *Biol. Reprod.* **36**, 1191–1198 (1987).
65. Y. Xia, G. M. Whitesides, Soft lithography. *Angew. Chem. Int. Ed. Engl.* **37**, 550–575 (1998).
66. G. Farnebäck, "Two-frame motion estimation based on polynomial expansion" in *Scandinavian Conference on Image Analysis*, J. Bigun, T. Gustavsson, Eds. (Springer, Berlin, 2003), pp. 363–370.
67. S. Kim, S. J. Karrila, *Microhydrodynamics: Principles and Selected Applications* (Courier Corporation, 2013).